The Astrophysical Journal, 977:244 (11pp), 2024 December 20 https://doi.org/10.3847/1538-4357/ad938b


# Fast Methods for Computing Photometric Variability of Eccentric Binaries: Boosting, Lensing, and Variable Accretion

Daniel J. D'Orazio[1,2], Paul C. Duffell[3], and Christopher Tiede[1]
[1] Niels Bohr International Academy, Niels Bohr Institute, Blegdamsvej 17, 2100 Copenhagen, Denmark; dorazio@stsci.edu, christopher.tiede@nbi.ku.dk
[2] Space Telescope Science Institute, 3700 San Martin Drive, Baltimore, MD 21218, USA
[3] Department of Physics and Astronomy, Purdue University, 525 Northwestern Avenue, West Lafayette, IN 47907-2036, USA; pduffell@purdue.edu
*Received 2024 March 10; revised 2024 October 30; accepted 2024 November 13; published 2024 December 18*

## Abstract

We analyze accretion-rate time series for equal-mass binaries in coplanar gaseous disks spanning a continuous range of orbital eccentricities up to 0.8 for both prograde and retrograde systems. The dominant variability timescales match those of previous investigations; the binary orbital period is dominant for prograde binaries with $e \gtrsim 0.1$, with a $5\times$ longer "lump" period taking over for $e \lesssim 0.1$. This lump period fades and drops from $5\times$ to $4.5\times$ the binary period as $e$ approaches 0.1, where it vanishes. For retrograde orbits, the binary orbital period dominates at $e \lesssim 0.55$ and is accompanied by a $2\times$ longer timescale periodicity at higher eccentricities. The shape of the accretion-rate time series varies with binary eccentricity. For prograde systems, the orientation of an eccentric disk causes periodic trading of accretion between the binary components in a ratio that we report as a function of binary eccentricity. We present a publicly available tool, `binlite`, that can rapidly ($\lesssim$0.01 s) generate templates for the accretion-rate time series onto either binary component for choice of binary eccentricity below 0.8. As an example use case, we build lightcurve models where the accretion rate through the circumbinary disk and onto each binary component sets contributions to the emitted specific flux. We combine these rest-frame, accretion-variability lightcurves with observer-dependent Doppler boosting and binary self-lensing. This allows a flexible approach to generating lightcurves over a wide range of binary and observer parameter space. We envision `binlite` as the access point to a living database that will be updated with state-of-the-art hydrodynamical calculations as they advance.

*Unified Astronomy Thesaurus concepts:* Accretion (14); Binary stars (154); Hydrodynamical simulations (767); Gravitational waves (678); Time domain astronomy (2109)

## 1. Introduction

The binary–gas-disk interaction arises in a multitude of astrophysical environments. It is important for binary orbital evolution (see, e.g., D. Lai & D. J. Muñoz 2023): from sculpting planetary system architectures (e.g., W. R. Ward 1997; R. P. Nelson 2018), to impacting stellar binary demographics (e.g., R. Valli et al. 2024), to facilitating mergers of stellar-mass (e.g., N. C. Stone et al. 2017) and supermassive (e.g., M. C. Begelman et al. 1980) black hole binaries (SMBHBs).

Gas disks also offer a way to observe such systems in the electromagnetic (EM) spectrum through accretion. In the realm of stellar binary+disk systems, radio and millimeter-wavelength observations have revealed a variety of disks feeding and forming young stellar binaries as well as planetary systems (e.g., J. J. Tobin et al. 2016; F. O. Alves et al. 2019; I. Czekala et al. 2021; A. Zurlo et al. 2023). In the time domain, photometric variability associated with periodic accretion onto stellar binaries has been observed in multiple systems (e.g., B. M. Tofflemire et al. 2017a, 2017b), providing further data on the disk+binary interaction.

Resolving disks around SMBHBs is more difficult than in the stellar case due to a lack of known subparsec-separation SMBHBs, uncertainty in the emission structure surrounding the accreting SMBHB at the relevant wavelengths, and the high spatial resolution needed for imaging of these distant sources (see D. J. D'Orazio & A. Loeb 2018, 2019). Similar to the stellar analog, however, accretion onto SMBHBs could be observable via bright, periodically modulated EM emission. While there is no definitive evidence for the subparsec-separation SMBHBs that will merge within the age of the Universe, accretion rates onto these systems can be as high as for single SMBHs (e.g., B. D. Farris et al. 2012; D. J. D'Orazio et al. 2013), suggesting that they could be a subpopulation of the quasars. In addition to being bright, such a binary-quasar population could be identified by its periodic imprint on quasar lightcurves, on ∼year or shorter timescales (Z. Haiman et al. 2009; L. Z. Kelley et al. 2021; C. Xin & Z. Haiman 2021; Z. Haiman et al. 2023). Such periodicity can arise from the binary's modulation of the accretion rate (e.g., K. Hayasaki et al. 2008; A. I. MacFadyen & M. Milosavljević 2008; D. J. D'Orazio et al. 2013; B. D. Farris et al. 2014) or observer-dependent relativistic effects due to the binary orbit (D. J. D'Orazio et al. 2015; D. J. D'Orazio & R. Di Stefano 2018; B. X. Hu et al. 2020). Both offer a way to identify such systems in photometric time-domain data, with multiple searches having identified ∼250 candidates to date (see D. J. D'Orazio & M. Charisi 2023, and references therein).

Time-domain searches require predictions for periodic signatures of binary accretion and also characterization of the intrinsic variability noise (e.g., S. Vaughan et al. 2016; X.-J. Zhu & E. Thrane 2020, for the SMBHB case). Here we make a step toward the former, by characterizing the variable accretion rates of eccentric binaries embedded in circumbinary disks (CBDs). We present an analysis of accretion variability measured from 2D isothermal numerical hydrodynamical

calculations of gas disks accreting onto equal-mass binaries for a continuous range of binary eccentricities $e \leqslant 0.8$ and for both prograde D'Orazio & Duffell (2021, hereafter DD21) and retrograde configurations of the binary and disk angular momentum Tiede & D'Orazio (2024, hereafter TD23). We use this data to build a publicly available tool named `binlite` (D. D'Orazio et al. 2024) that can rapidly generate accretion-rate time-series data for any binary eccentricity in the simulated range via Fourier decompositions of the simulation data.

Section 2 describes our methods, while Sections 3.1, 3.2, and 3.3 present the results of our periodicity analysis, accretion-rate time series reconstruction, and calculation of preferential accretion rates. As an example use case and to demonstrate the wide range of periodic lightcurves that can arise from accreting eccentric binaries, Section 4 presents a method for generating lightcurves of accreting black hole binaries in a chosen observing band, while including the observer-dependent relativistic effects of Doppler boosting and gravitational self-lensing for multiple observer viewing angles.

We envision this tool and the data it is built from as a starting point from which further sophistication in numerical models and postprocessing can be added with the goal of generating a publicly available, living-lightcurve database for modeling, interpreting, and searching for emission from accreting binary systems. We discuss these future prospects and current limitations in Section 5.

## 2. Methods

Throughout we consider a binary of total mass $M$, with equal-mass components (described by mass ratio $q \equiv M_2/M_1 = 1$), orbital eccentricity $e$, semimajor axis $a$, and orbital angular frequency $\Omega_b$. A locally isothermal CBD accretes onto the binary and is modeled with viscous hydrodynamics in the two dimensions in the plane of the binary orbit. In this case the disk is characterized by the disk aspect ratio in vertical hydrostatic equilibrium $h$, which describes the relative importance of pressure forces, and the kinematic coefficient of viscosity $\nu$. Because of the simplified physics, one can scale results to any value of $M$ or $a$, which amounts to choosing an orbital timescale via $\Omega_b$. Throughout we scale the accretion rate by the equivalent steady-state value for a single mass, $\dot{M}_0 = 3\pi\Sigma_0\nu$, for arbitrary surface-density scale $\Sigma_0$. We consider both prograde and retrograde configurations of the binary orbit with respect to the CBD. In both cases the equations of hydrodynamics are solved using the moving-mesh code `DISCO` (P. C. Duffell 2016).

*Accretion From a Prograde CBD.* The accretion-rate time-series data for prograde disks around eccentric binaries are taken directly from the output of 2D numerical viscous hydrodynamical calculations described in DD21. These calculations assume a locally isothermal equation of state, which keeps the aspect ratio a constant value of $h = 0.1$ in the CBD and a spatially constant coefficient of kinematic viscosity $\nu = 10^{-3}a^2\Omega_b$. Specifically, we utilize the main calculations in DD21, which evolve the binary and disk for 25,000 binary orbits, with the first 500 orbits relaxing the disk around a binary on a circular orbit and the following 20,000 binary orbits sweeping the binary eccentricity linearly from $e = 0$ to $e = 0.9$. Here we utilize the accretion rates measured via a sink prescription (Equation (3) of DD21) onto each component of the binary as a function of time.

*Accretion From a Retrograde CBD.* The accretion-rate time-series data for retrograde disks around eccentric binaries are taken directly from the output of 2D numerical viscous hydrodynamical calculations described in TD23. These calculations assume the same disk and binary parameters as the prograde case except that the binary eccentricity is swept linearly from $e = 0.0$ to 0.8 over a timescale of 10,500 orbits, with 500 orbits to relax the disk around a binary with a circular orbit. We note that the accretion sinks in TD23 have half the characteristic sink size and are implemented to be "torque free," compared to the standard sink implementation in DD21 (see A. M. Dempsey et al. 2020; A. J. Dittmann & G. Ryan 2021, for further clarification on these sink types).

### 2.1. Accretion-rate Variability Timescales

We first compute the dominant variability timescales as a function of binary orbital eccentricity. We follow P. C. Duffell et al. (2020) and TD23 and compute a 2D periodogram of the accretion-rate time series by taking the norm of the quantity,

$$\mathcal{P}(e,\,\omega) = \frac{1}{\sqrt{2\pi\sigma_{\mathcal{P}}^2}}\int_{t(e_0)}^{t(e_f)} \mathrm{e}^{-\frac{1}{2}\frac{(t(e)-\tau)^2}{\sigma_{\mathcal{P}}^2}}\dot{M}(\tau)\mathrm{e}^{-i\omega\tau}d\tau, \qquad (1)$$

which picks out the power in Fourier components with frequency $\omega$ in a window of the accretion-rate time series centered on time $t(e)$ and of characteristic width $2\sqrt{2\log 2}\,\sigma_{\mathcal{P}}$. For our choice of $\sigma_{\mathcal{P}} = 30(2\pi\Omega_b^{-1})$, this corresponds to a small window of $\sim$70 orbits in eccentricity centered around any $e$ in the time series.

### 2.2. Fourier Reconstruction

Our primary goal is to generate accretion-rate time series, which are periodic over the binary orbital period, for any chosen value of the orbital eccentricity. This is possible given the continuous sweep of our solutions through binary parameter space. We start with the total accretion rate onto the binary $\dot{M}(t)$ and its two components $\dot{M}_1(t)$ and $\dot{M}_2(t)$ computed over the entire 25,000 (10,500) orbit sweep from the numerical calculation of DD21 (TD23). Because these calculations carried out a linear sweep in eccentricity with time, we also have a linear relation between the time $t$ and the orbital eccentricity, $t(e)$.

The accretion-rate time series at a given orbital eccentricity, onto either component of the binary, is reconstructed with a Fourier series,

$$\dot{M}_{\mathrm{Rec}}(t,\,e) = \alpha_0 + \sum_n \alpha_n(e)\cos(n\Omega t) + \sum_n \beta_n(e)\sin(n\Omega t), \qquad (2)$$

for chosen fundamental frequency $\Omega$ and its integer multiples. That is, a simple yet accurate reconstruction is possible when the primary power is concentrated at integer multiples of one frequency. A natural choice is the binary frequency $\Omega_b$, and we show in Section 3.1 that this is indeed the best choice except for a few regions of parameter space where a lower frequency dominates, but still at approximate integer multiples of $\Omega_b$.

The Fourier amplitudes are computed for the nearly continuous range of orbital eccentricities by convolving the accretion-rate time series with a Gaussian centered around a

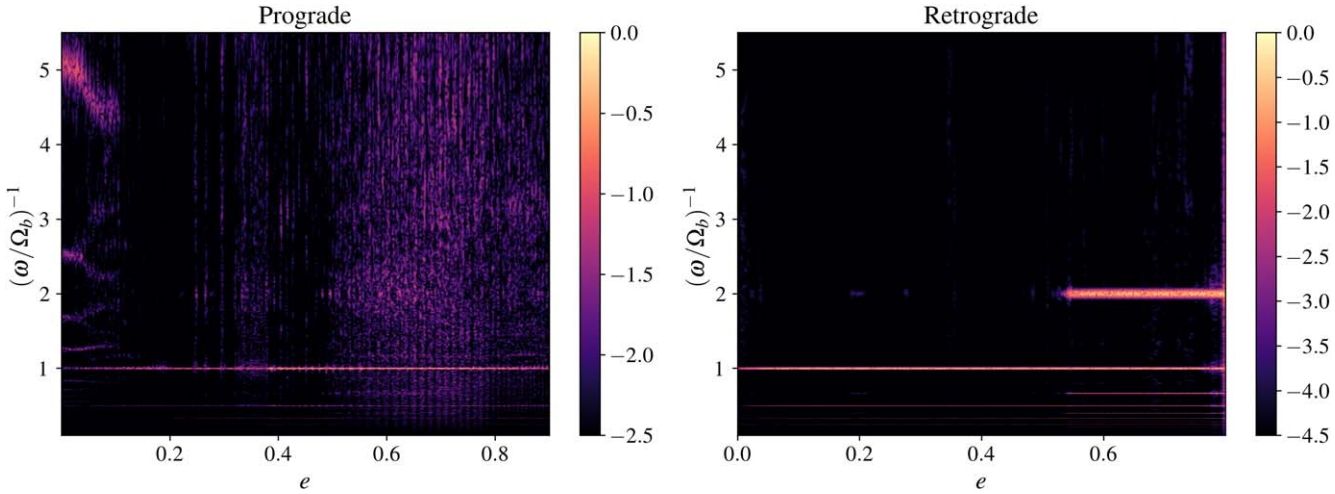


**Figure 1.** The 2D periodograms of the total accretion rate from prograde (left) and retrograde (right) CBDs onto binaries with orbital eccentricity $e$ ranging from 0.0 to 0.8. The $y$-axis indicates the timescale in units of orbital periods. Black indicates regions where there is low power (see color bars), while purple and yellow regions have increasingly more power (on a $\log_{10}$ scale).

chosen eccentricity $e$ that arises at time $t(e)$ in the eccentricity sweep:

$$\alpha_0(e) = \frac{1}{\sqrt{2\pi\sigma^2}} \int_{t(e_0)}^{t(e_f)} \dot{M}(t') e^{-\frac{1}{2}\left[\frac{(t'-t(e))^2}{\sigma^2}\right]}\, dt' \tag{3}$$

$$\alpha_n(e) = \frac{2}{\sqrt{2\pi\sigma^2}} \int_{t(e_0)}^{t(e_f)} \dot{M}(t') e^{-\frac{1}{2}\left[\frac{(t'-t(e))^2}{\sigma^2}\right]} \cos(n\Omega t')\, dt'$$

$$\beta_n(e) = \frac{2}{\sqrt{2\pi\sigma^2}} \int_{t(e_0)}^{t(e_f)} \dot{M}(t') e^{-\frac{1}{2}\left[\frac{(t'-t(e))^2}{\sigma^2}\right]} \sin(n\Omega t')\, dt',$$

where $\sigma$ chooses the window width of $\dot{M}$ times-series data over which to construct the Fourier series. In practice, we calculate reconstructions up to $e = 0.81$ for prograde systems and $e = 0.791$ for retrograde systems. Throughout we choose $\sigma = 10(2\pi\Omega_b^{-1})$, which corresponds to a Gaussian full width at half-maximum of ≈23.5 orbits.

Tracking accretion rates onto both components of an equal-mass-ratio binary is necessary because, for prograde disks, some binary eccentricities excite disk eccentricities that allow the (orbit-averaged)[4] accretion rate to periodically favor one binary component over the other (A. C. Dunhill et al. 2015; D. J. Muñoz & D. Lai 2016; M. Siwek et al. 2023b). The simulations of DD21 find that for $0.0 \leqslant e \leqslant 0.18$ and $e \geqslant 0.38$ the cavity is eccentric and precesses on superorbital timescales ($\mathcal{O}(10^2)$ orbital periods). This causes the accretion to favor one binary component for approximately one half of the precession period of the eccentric cavity. When binary and cavity eccentricity vectors pass through a perpendicular configuration, the accretion-rate ratio quickly swaps to favor the other component for the other half of the cavity precession period. Hence, when the circumbinary cavity is eccentric and precessing, for prograde disks around binaries with eccentricities in the range $0.0 \leqslant e \leqslant 0.18$ and $e \geqslant 0.38$, there are three possible accretion states: one where the primary dominates accretion, one where the secondary dominates accretion, and one shorter-lived state where the two share the accretion rate as they swap between the first two states. In these cases the accretion-rate ratio averages to unity when taken over a disk precession period.

DD21 finds that prograde disks around binaries with eccentricities in the range $0.18 \leqslant e \leqslant 0.38$ are much more symmetric around the origin and either do not precess (due to lack of disk eccentricity or to locking with the binary eccentricity vector) or have much longer precession periods than for higher or lower binary eccentricities. Similar observations were made from the numerical calculations of R. Miranda et al. (2017) and M. Siwek et al. (2023b). M. Siwek et al. (2023b) classify regions of parameter space where the disk eccentricity is "locked" to the binary eccentricity, finding such a state for $e = 0.2$, $q = 1$, and otherwise finding precessing states for $e = 0.0$, 0.4, 0.6, and 0.8, in agreement with DD21. Here we find[5] that even in the locked regime, the small asymmetry of the disk can still cause the accretion rate to be split unequally between the binary components, but with a different nature than for the precessing solutions. While the eccentric binary–disk dynamics are worth understanding further in this regime, for the purposes of this study, we note that even in this "symmetric" nonprecessing disk state, asymmetries arise that cause unequal accretion rates onto the binary components (see Section 4).

For retrograde systems, where persistent disk eccentricities are not excited, the accretion rates are always split evenly between the binary components.

## 3. Results

### 3.1. Periodicity Analysis

*Prograde Periodogram.* The left panel of Figure 1 shows $\log_{10}|\mathcal{P}(e, \omega)|$ for prograde accretion computed via Equation (1) over a grid of 600 × 600 values of $\omega$ and $e$. Bright colors denote significant power, while dark colors denote lack of power at that corresponding point in parameter space[6]—the $y$-axis indicates the periodicity timescale in units of the binary orbital period, and the $x$-axis indicates binary eccentricity.

[4] Intraorbital preferential accretion variations are revealed in the accretion-rate time series below.

[5] As first reported from analysis of the DD21 data set here.

[6] To distinguish strong periodic signatures from orders-of-magnitude lower-power noise in the simulation data, we set a minimum displayed power, denoted by the color bar in each panel.

For $e \lesssim 0.1$ we find that, in agreement with previous works (*e.g.,* D. J. Muñoz & D. Lai 2016; R. Miranda et al. 2017; J. Zrake et al. 2021), the power is concentrated at the orbital period and its harmonics but is dominant in a small range of timescales centered around five binary orbital periods. This corresponds to the timescale for the cavity "lump" to circulate and periodically alter the feeding rate to the binary (A. I. MacFadyen & M. Milosavljević 2008; D. J. D'Orazio et al. 2013). Previous $e = 0$ and $q = 1$ studies found that, in addition to a dominant "lump" timescale, symmetry leads to decreased power at the orbital periodicity compared to half-orbital (e.g.,D. J. D'Orazio et al. 2013; D. J. Muñoz et al. 2019; P. C. Duffell et al. 2024).[7] The left panel of Figure 1 shows that the orbital power does decrease slightly for small $e$ but does not completely disappear, nor is it superseded by the half-orbital power. However, because our periodogram is taken over a sliding window in $e$, we do not exactly probe $e = 0$, and the left panel of Figure 1 suggests that limiting $e = 0$ behavior may appear only at very small $e$.

For $0.05 \lesssim e \lesssim 0.1$, power in the "lump timescale" splits into branches centered on the five-binary-orbit feature. This branching can be seen most easily in the higher frequency ($1/2.5P_b^{-1}$) harmonic of the lump timescale on the left side of the left panel of Figure 1. The dominant lump branch drops in frequency from $1/5P_b^{-1}$ to $1/4.5P_b^{-1}$ as $e$ increases from $0.05 \rightarrow 0.1$. At $e = 0.1$ the lump branches vanish and are replaced by power that is almost entirely focused at the orbital timescale and its higher harmonics. Orbital period timescales then dominate for $e \gtrsim 0.1$. At higher orbital eccentricities, particularly for $0.5 \lesssim e \lesssim 0.8$, the power is noisy at lower frequencies. This arises due to less stability in the accretion-rate time series from orbit to orbit. We demonstrate this further in the next section.

Our primary takeaway for the purpose of generating reconstructions of the accretion-rate time series is that the orbital period is a dominant feature for all eccentricities $e \geqslant 0.1$; hence, we choose $\Omega_b$ as our fundamental frequency for the Fourier reconstruction—Equations (2) and (3). For $e < 0.1$, we choose $\Omega_b/5$ as the fundamental frequency but with more terms in the reconstruction.

*Retrograde Periodogram*. The right panel of Figure 1 shows $\log_{10}|\mathcal{P}(e, \omega)|$ for retrograde accretion computed via Equation (1) over a grid of $600 \times 600$ values of $\omega$ and $e$. A different version of this is also published and explained further in TD23 (over a different range of timescales). Our main purpose for showing it here is to emphasize that the orbital timescale periodicity is strong for all eccentricities. However, in the retrograde case, an equally strong but less temporally concentrated two-times-orbital periodicity arises for $e \sim 0.55$. Hence, for retrograde systems we choose the fundamental Fourier reconstruction frequency to be $\Omega_b/2$. Note that the retrograde periodogram is much less noisy than its prograde counterpart, indicating steadier accretion-rate times series, even for high eccentricities.

### 3.2. Accretion-rate Time Series

*Prograde Time Series*. Figure 2 presents example accretion-rate time series for prograde binaries with eight different values of orbital eccentricity. The solid lines show the accretion rates measured directly from the numerical calculations, while the dashed lines are the accretion templates built from our Fourier reconstruction (Equations (2) and (3)) using $\Omega = \Omega_b$ and a total of 30 Fourier components. Accretion rates onto each component are denoted in coral and teal, while the total is plotted in black. Vertical dotted lines denote the time of pericenter, while vertical dotted–dashed lines denote apocenter. Note that even though we have included enough Fourier components to capture sharp features in the time series (e.g., the bottom-right panel of Figure 2), small deviations between the reconstructions (dashed) and the simulation (solid) are apparent for $e \gtrsim 0.5$. This is due to the interorbit variability, which manifests as the noisy upper-right region in the prograde periodogram (left panel) of Figure 1, i.e., at some eccentricities the accretion rate is less steady from one orbit to the next, affecting our reconstructions, which are built from an average over $\sim$20 orbits. For the highest plotted eccentricity ($e = 0.8$), however, the very close binary pericenter passage generates a steady and prominent accretion spike (bottom-right panel of Figure 1), bringing enhanced interorbit consistency to the accretion-rate time series and improving the template match. Note also the appearance of smaller, irregular accretion spikes between the pericenter spikes for $e \gtrsim 0.5$, found also in J. Zrake et al. (2021).

Figure 3 demonstrates a reconstruction for a prograde binary with $e = 0.01$, where the $\omega \sim \Omega_b/5$ periodicity of the cavity lump dominates. In this case the Fourier reconstruction uses $\Omega = \Omega_b/5$ and 60 Fourier components. Here, the more complex nature of the variability is apparent in the less exact match of reconstruction and direct simulation (see again the more complex structure in the $e < 0.01$ portion of the left periodogram in Figure 1). Despite this, the reconstruction captures the main qualitative features of the time series, including, crucially, the periodicity at both $2\Omega_b$ and $\Omega_b/5$ and reliable reconstruction of the contribution of each component accretion rate to the total.

*Retrograde Time Series*. Figure 4 shows the reconstructed total, primary, and secondary accretion rates for retrograde binary–disk systems using $\Omega = \Omega_b/2$ and 30 terms in the Fourier reconstruction. The reconstructed and simulated cases capture both orbital and twice-orbital periodicity very well and result in nearly identical reconstructed-versus-simulated curves. This is due to the much more steady nature of retrograde disk solutions across the parameter space. The total retrograde accretion rates are described further in TD23, while here we additionally show the component accretion rates. These are nearly identical to each other, as is expected for equal-mass binaries when no other asymmetry arises, i.e., the eccentric disk of the prograde case.

### 3.3. Accretion-rate Ratio Q

Over long enough timescales ($\mathcal{O}(10^2 - 10^3)$ binary orbits), the accretion rates onto equal-mass binaries will average to unity (e.g., M. Siwek et al. 2023a).[8] However, when computing lightcurves, the relevant quantity is the accretion-rate ratio between the binary components over timescales spanning orbital periods. To quantify this, we define the ratio

[7] See also A. Franchini et al. (2023), who show that the orbital periodicity can be shifted when considering a live binary.

[8] Though this seems not be the case when binary eccentricity and disk eccentricity vectors are locked relative to each other, as could be the case for our $e \sim 0.2$ results—this requires further investigation.

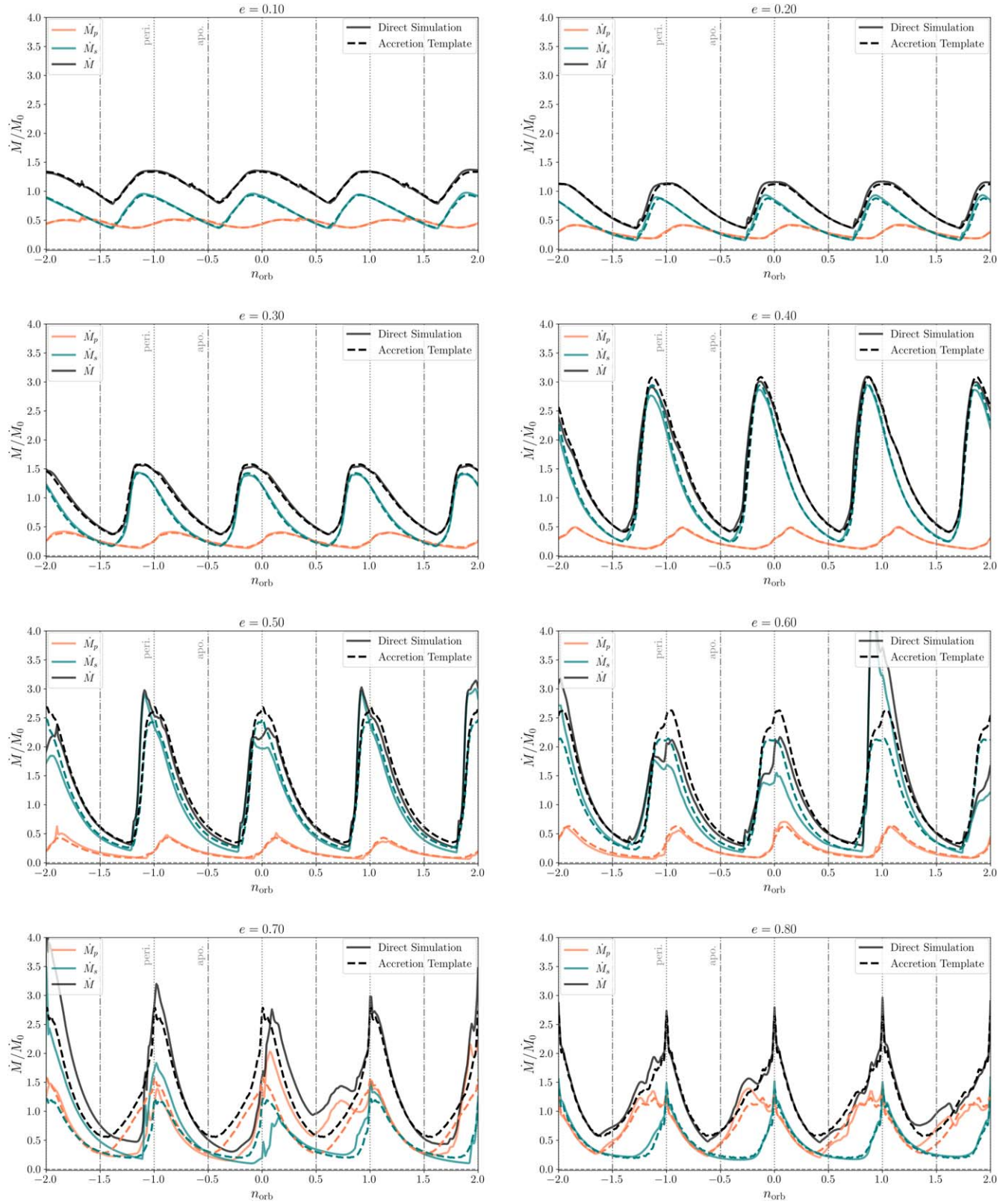


**Figure 2.** Match of accretion-rate templates constructed with our code `binlite` (dashed curves) compared to the simulation output (solid curves). The total accretion rate onto the binary is plotted in black, while the breakdown of accretion onto each binary component is represented by the coral and teal curves. Accretion rates are plotted in units of the steady-state value $\dot{M}_0$. The time series is displayed over 4 binary orbits comprising the center of a $\sim$20 orbit segment from which the Fourier reconstruction is built. Deviations between the reconstruction and simulation output for $e = 0.5$, 0.6, and 0.7 derive from interorbital variability (peak-to-peak variations), whose presence is apparent from the noisy region in the top-right portion of the corresponding periodogram in Figure 1. The binary components have equal masses, but the eccentric cavity causes preferential accretion that could equivalently be favoring either black hole. Hence, labeling of coral and teal curves can be interchanged.

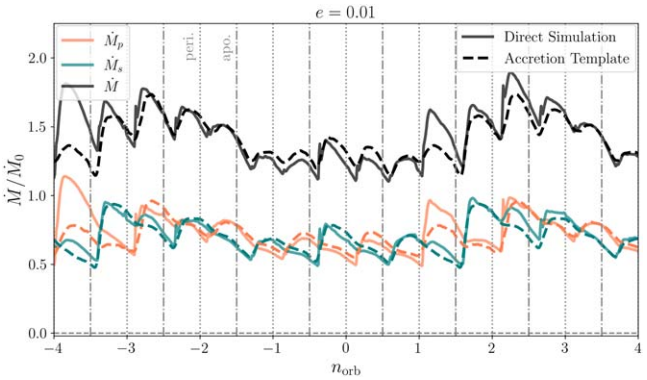


**Figure 3.** The same as Figure 2 but for a prograde, $e = 0.01$ system, where variability at $2\Omega_b$ and $\Omega_b/5$ coexist.

$Q = \langle \dot{M}_2/\dot{M}_1 \rangle$, averaged over an integer number of orbits for which the eccentric accretion-rate imbalance operates (much shorter than a disk precession timescale).

The ratio of component accretion rates, $Q$ is always unity for retrograde, equal-mass binaries (see Figure 4) but is a function of eccentricity for prograde binaries. In Figure 5 we present $Q$ measured from the prograde simulations as a function of binary eccentricity. The gray x's represent 1000 values drawn from the reconstructed accretion rates averaged over five orbits, sampled evenly in $e$. Because preferential accretion trades between primary and secondary, we present the minimum of $Q$ and $Q^{-1}$, with both values being valid choices when modeling equal-mass binaries considered here. When plotted this way, the extreme values of the ratio of accretion rates can be approximated by a simple function of eccentricity, inspired by the ratio of pericenter and apocenter distances of the binary components,

$$\begin{aligned} Q_{\rm min} &\approx \frac{1 - \mathcal{P}(e)e}{1 + \mathcal{A}(e)e} \\ \mathcal{P}(e) &= 2 - e^2 - 2e^3 \\ \mathcal{A}(e) &= 2 + e^2, \end{aligned} \tag{4}$$

which is drawn as the solid blue line in Figure 5.

For most binary eccentricities the accretion-rate periodically switches back and forth between favoring each of the binary components. Hence, the ratio of accretion rates used to compute lightcurves can take values between $Q_{\rm min}$ and $Q_{\rm min}^{-1}$. As can be seen from the density of gray x's in Figure 5, the binary spends more time accreting at some ratios than others: $Q = 1$ is sparsely sampled because this value is encountered during the relatively rapid stage where the accretion rate switches from favoring one component to favoring the other. The black points and associated error bars show the average accretion ratio from a set of constant-eccentricity verification runs (detailed in DD21), and the black triangles illustrate the smallest value over the run. Those values of $Q$ that lie within the error bars from these constant-eccentricity runs provide a good indicator for where the binary spends most of its time accreting.

For intermediate values of eccentricity, the disk is more symmetric around the origin and is either slowly precessing or not precessing at all. This results in regions with narrow spreads of accretion-rate ratio $Q$, seen as the clustering of gray x's between $0.018 \lesssim e \lesssim 0.38$ in Figure 5. While the spread of $Q$ values is much smaller in this range than outside of it, $Q$ is not continuous in $e$ here and jumps through four different states of monotonically varying $Q(e)$, while also experiencing islands of oscillating disk solutions near the transitions between these four states. This behavior is likely due to locking of the angle between disk and binary eccentricity and would be worth studying further for elucidating the binary+disk dynamics in this regime and its relation to observability via, e.g., accretion variability.

## 4. Application: Construction of Boosted and Lensed Lightcurves

As an example use case and to demonstrate the wide range of lightcurve shapes that can arise from accreting, eccentric binaries, we develop a simple procedure for converting the accretion-rate time series of the previous section to a rest-frame flux. Primarily for application to accreting black hole binaries, we then convert this to an observer-dependent flux by including relativistic orbital Doppler boosting of emission emanating from the minidisks around each binary component (D. J. D'Orazio et al. 2015), as well as binary self-lensing in the point-mass, point-source limit (D. J. D'Orazio & R. Di Stefano 2018; B. X. Hu et al. 2020).

Doppler boosting and binary lensing have been put forth as mechanisms for causing unique periodic variability in accreting SMBHB systems (D. J. D'Orazio et al. 2015; D. J. D'Orazio & R. Di Stefano 2018; B. X. Hu et al. 2020; J. Davelaar & Z. Haiman 2022; A. Ingram et al. 2021; D. J. D'Orazio & M. Charisi 2023; L. M. Krauth et al. 2024), with positive prospects for detection with upcoming EM surveys (e.g., L. Z. Kelley et al. 2021; C. Xin & Z. Haiman 2021; C. A. Witt et al. 2022; Z. Haiman et al. 2023; K. Park et al. 2024) as well as multimessenger approaches (e.g., M. Charisi et al. 2022; C. Xin & Z. Haiman 2024). Modeling these signatures consistently requires knowledge of the fraction of light coming from each of the minidisks and the CBD. It should also be combined with the intrinsic variability of the source in order to understand systems where both hydrodynamical variability as well as observer-dependent effects are jointly operating.[9] Hence, the reconstructed accretion-rate time series of the previous section allow us to significantly build upon toy models for the variability of accreting SMBHBs.

We model the emission from the accreting binary in a given frequency band as a constant specific flux from the CBD, $F^0_{\nu,\rm CBD}$, plus time-dependent emission from the primary and secondary minidisks. We model the minidisk emission as a constant, average flux times a time-dependent function $F^0_{\nu,1}p(t)$ and $F^0_{\nu,2}s(t)$, where $p(t) \equiv \dot{M}_1/\langle \dot{M}_1 + \dot{M}_2 \rangle$ and $s(t) \equiv \dot{M}_2/\langle \dot{M}_1 + \dot{M}_2 \rangle$ are the reconstructed time-variable accretion rates computed with `binlite` (Section 3.2) and normalized by the average total accretion rate at that eccentricity.

*Lightcurve Generation.* With boosting and lensing taken into account the total observed flux is

$$\begin{aligned} F_\nu = &F^0_{\nu,1}\mathcal{D}_1\mathcal{M}_1 p(t) \\ &+ F^0_{\nu,2}\mathcal{D}_2\mathcal{M}_2 s(t) + F^0_{\nu,\rm CBD}, \end{aligned} \tag{5}$$

where $\mathcal{D}_i \equiv D_i^{3-\alpha}$ is the time-dependent Doppler-boost magnification for Doppler factor $D_i$ and frequency-dependent log-spectral slope $\alpha$ in the observing band (assumed here to be the same for all disk components), while $\mathcal{M}_i$ is the time-

[9] A combination of Doppler boosting and hydrodynamic variability near the merger is simulated in Y. Tang et al. (2018).

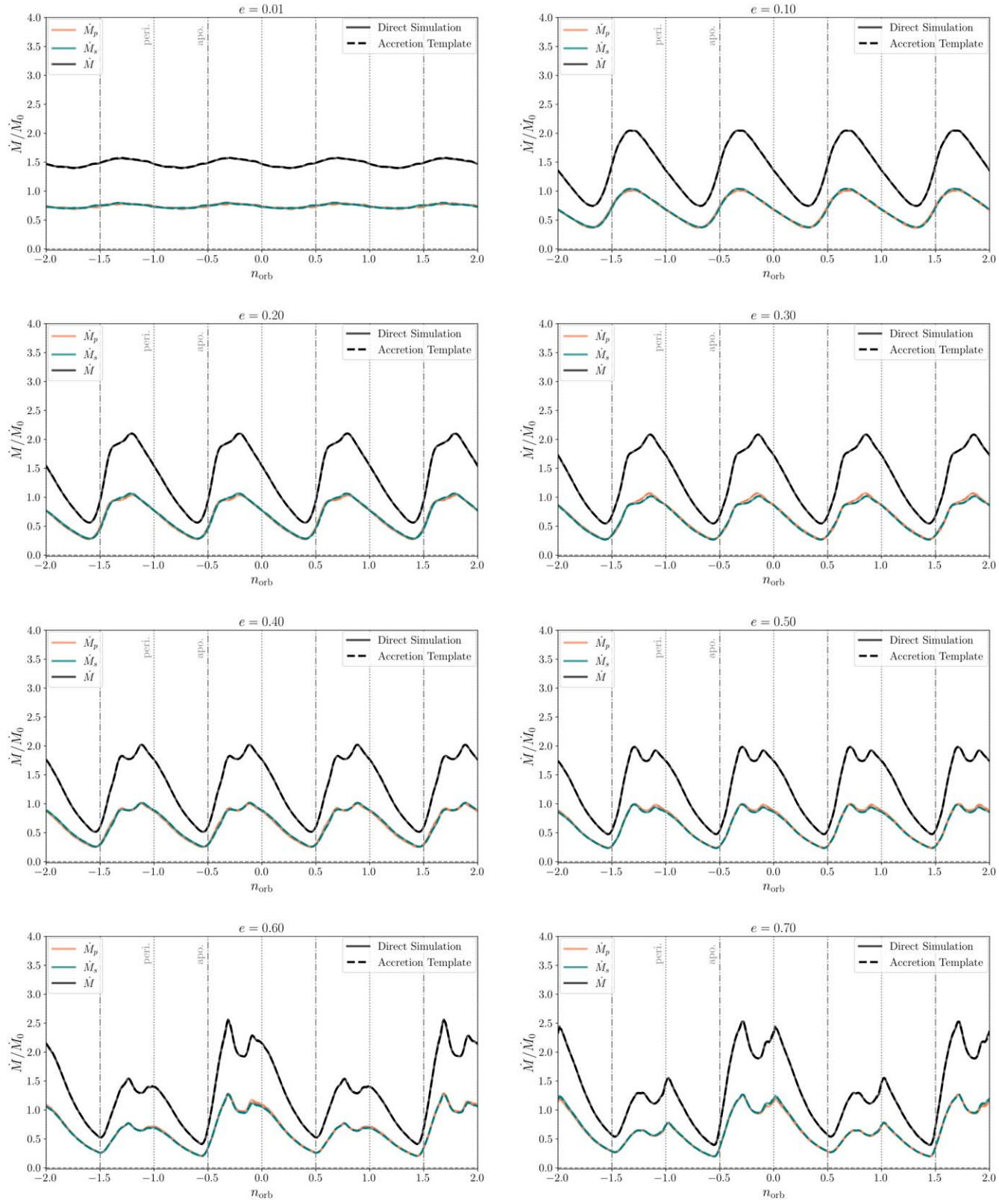


**Figure 4.** The same as Figure 2 but for retrograde, eccentric binaries. Here the accretion rates onto the primary (coral) and secondary (teal) are nearly identical because there is no precessing, circumbinary cavity.

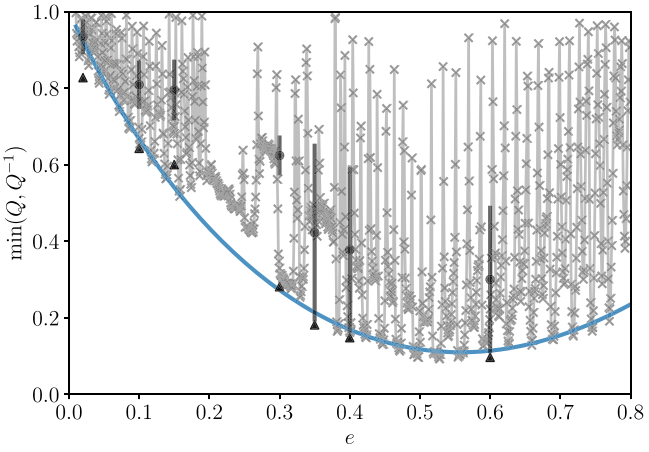


**Figure 5.** The ratio $Q \equiv \langle \dot{M}_2/\dot{M}_1 \rangle$ of accretion rates onto each binary component, averaged over a duration shorter than the disk precession frequency. The gray x's are measured from our reconstruction, while the blue line is an analytic approximation for the extreme values. As a check of the values derived from the eccentricity sweep, the black points show results measured from all DD21 simulations with fixed eccentricities—black points with error bars represent the average and standard deviation of $\min(Q, Q^{-1})$ over a precession period of the disk , and the triangles denote the smallest values over the same range.

dependent lensing magnification for the specified binary component (see D. J. D'Orazio & R. Di Stefano 2018; B. X. Hu et al. 2020). Defining

$$\begin{aligned} F^0_{\nu,\mathrm{Tot}} &\equiv F^0_{\nu,1} + F^0_{\nu,2} + F^0_{\nu,\mathrm{CBD}}, \\ \chi_{\nu,1} &\equiv F^0_{\nu,1}/F^0_{\nu,\mathrm{Tot}}, \\ \chi_{\nu,2} &\equiv F^0_{\nu,2}/F^0_{\nu,\mathrm{Tot}}, \end{aligned} \tag{6}$$

we can write the observed in-band flux, normalized to the total average (rest-frame) flux, as

$$\begin{aligned} \frac{F_\nu}{\langle F^0_{\nu,\mathrm{Tot}} \rangle} &= \chi_{\nu,1}\mathcal{D}_1\mathcal{M}_1 p(t) + \chi_{\nu,2}\mathcal{D}_2\mathcal{M}_2 s(t) \\ &\quad + (1 - \chi_{\nu,1} - \chi_{\nu,2}), \end{aligned} \tag{7}$$

which reduces to

$$\frac{F_\nu}{\langle F^0_{\nu,\mathrm{Tot}} \rangle} = (1 - \chi_{\nu,2})\mathcal{D}_1\mathcal{M}_1 p(t) + \chi_{\nu,2}\mathcal{D}_2\mathcal{M}_2 s(t), \tag{8}$$

for a simplified case where the minidisks are assumed to outshine the CBD.

Hence, we need to know the relative fluxes, in a specified frequency band, from each minidisk and the CBD. This requires knowing the disk spectra, which depends on physics of radiative energy balance in the accretion flow not captured by our isothermal simulations. For simplicity, we treat the CBD and both minidisks as separate components and approximate the spectra of each component with composite blackbody spectra of the optically thick alpha-disk solutions. In this case, the spectrum is set by each disk temperature profile, $T(r) \propto (M\dot{M}/r^3)^{1/4}$, which for equal-mass binary components differs between minidisks only through the accretion rate and by an extra mass factor $2^{1/4}$ for the CBD surrounding the total binary mass.

This allows us to compute spectra of each of the disk components by choosing a total accretion rate through the CBD, a binary mass ratio, and using the split in accretion rates onto the binary components measured from the reconstructed accretion rates of Section 3. Over long enough timescales, the average accretion rate through the CBD is split evenly for equal-mass binary components. However, as discussed in Sections 3.2 and 3.3, for prograde eccentric binaries, this balance can be shifted back and forth between components over periods of $\mathcal{O}(100)$ binary orbits as the eccentric disk precesses with respect to the binary argument of pericenter. To quantify this, we use the accretion-rate ratio explored in Section 3.3 and Figure 5, $Q \equiv \langle \dot{M}_2/\dot{M}_1 \rangle$. We require that the minidisks are fed by a CBD with total mass-accretion rate $\dot{M}_{\mathrm{CBD}}$. Then the measured $Q$ and choice of $\dot{M}_{\mathrm{CBD}}$ specify the system:

$$\dot{M}_1 = \dot{M}_{\mathrm{CBD}}(1 + Q)^{-1}; \quad \dot{M}_2 = Q\dot{M}_1, \tag{9}$$

so that, evaluated at the same radius,

$$T_{\mathrm{CBD}} = 2^{1/4}(1 + Q)^{1/4} T_1; \quad T_2 = Q^{1/4} T_1, \tag{10}$$

where we have assumed that the binary components have equal masses in the second line. The average fluxes from each disk component are

$$\begin{aligned} F^0_{\nu,1} &= \frac{2\pi \cos I}{d^2} \int_{r_{i,1}}^{r_{o,1}} B_\nu \left[ T_{i,1} \left( \frac{r}{r_{i,1}} \right)^{-3/4} \right] r dr \\ F^0_{\nu,2} &= \frac{2\pi \cos I}{d^2} \int_{r_{i,2}}^{r_{o,2}} B_\nu \left[ Q^{1/4} T_{i,1} \left( \frac{r}{r_{i,1}} \right)^{-3/4} \right] r dr \\ F^0_{\nu,\mathrm{CBD}} &= \frac{2\pi \cos I}{d^2} \int_{r_{i,\mathrm{CBD}}}^{r_{o,\mathrm{CBD}}} B_\nu \\ &\quad \times \left[ 2^{1/4}(1 + Q)^{1/4} T_{i,1} \left( \frac{r}{r_{i,1}} \right)^{-3/4} \right] r dr, \end{aligned} \tag{11}$$

for a source at distance $d$ and a common disk inclination angle $I$. For the examples here, we assume that the CBD extends from $r_{i,\mathrm{CBD}} = 2a$ to $r_{o,\mathrm{CBD}} = 100a$ and that the minidisks extend from the Schwarzschild innermost stable circular orbit of the black hole, e.g., $r_{i,1} = 6GM_1/c^2$, to the tidal truncation radius, $r_0 \approx 0.27a = 0.27(\Omega_b)^{-2/3}(GM)^{1/3}$ (C. Roedig et al. 2014). The quantity $T_{i,1}$ is the temperature in the primary minidisk at $r_{i,1}$. We emphasize that in this model, Equation (11) sets the average flux scale for each disk component, while time variability comes from the `binlite` accretion-rate time series of Section 3.2.

*Example Lightcurves.* We compute example lightcurves in the $V$ band (optical) for different binary viewing angles and eccentricities in Figures 6 and 7. For these examples we choose binary parameters $M = 2 \times 10^9 M_\odot$ and $P = 1$ yr, place the source at a luminosity distance of 1.5 Gpc ($z \approx 0.29$), and prescribe a total accretion rate onto the binary of 10% of the Eddington rate, with 10% accretion efficiency. To set the amplitude of Doppler-boost variability we choose a spectral index in the observing band of $\alpha = -1$ (see, e.g., M. Charisi et al. 2018) and keep $\cos I = 1$ fixed for easy comparison throughout. For the accretion-rate ratio we use Equation (4). For an eccentricity of $e = 0.4$, this results in a value of $Q = 0.169$, and $V$-band flux ratios of $\chi_{V,1} = 0.308$ and $\chi_{V,2} = 0.160$. Hence, in this example, the minidisks are

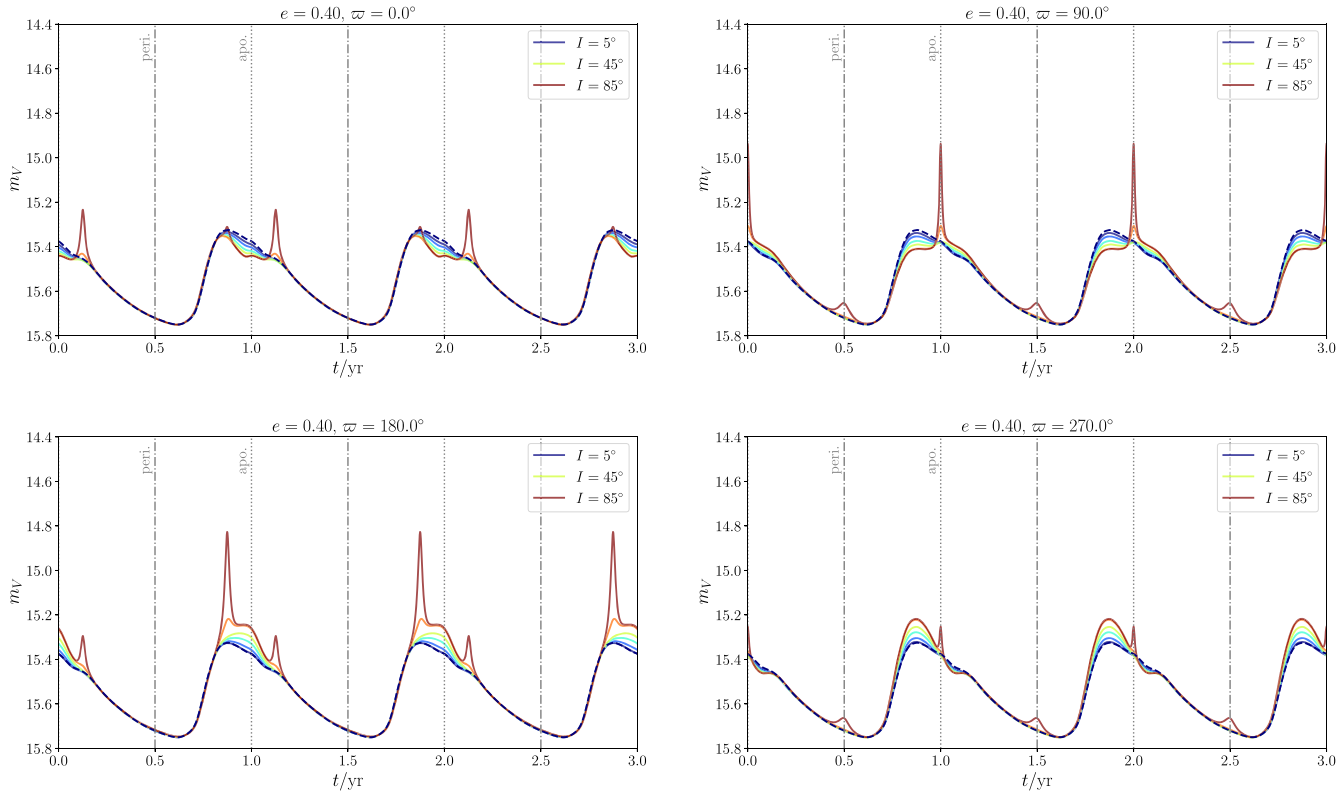


**Figure 6.** *V*-band apparent magnitude lightcurves for prograde systems (see Section 4). Each panel is drawn for a different azimuthal viewing angle of the binary orbit relative to the argument of pericenter $\varpi$, and each differently colored line is for a different binary inclination to the line of sight. The dashed line represents a face-on binary and so exhibits purely accretion-rate-induced flux variability (compare to Figure 2). The strongest Doppler and lensing effects arise for the red line, drawn for a binary inclined close to the line of sight, $I = 85°$. Each panel assumes a binary with $M = 2 \times 10^9 M_\odot$ and $P = 1$ yr, at a distance of 1.5 Gpc, and accreting at 10% of the Eddington rate.

contributing ≈53% of the total *V*-band flux. Note that this relative contribution can be a strong function of observing band, binary masses, and accretion rate, ranging from 0 to 1. We compute the flux in the *V* band, $F_V(t)$, by multiplying Equation (7) by the sum of Equation (11) evaluated at $\nu = 5.5 \times 10^{14}$ Hz and then computing an approximate *V*-band apparent magnitude $m_V = -2.5 \log_{10}[F_V(t)/F_{V,0}]$, using the *V*-band zero-point flux of $F_{V,0} = 3630.22$ Jy.

Figures 6 and 7 show that a wide range of lightcurve morphologies arise when allowing viewing angle and eccentricity to vary. It is significant that each lightcurve is uniquely fixed by binary and observer parameters. Specifically, the Doppler+lensing-induced and accretion-rate-induced features cannot be shifted in phase independently of one another. This is because both accretion-rate and the Doppler+lensing variability have features fixed to specific values of the binary phase. The peaks and troughs of the Doppler-boost modulation (as well as its shape) and the lensing flares occur at unique values of the binary phase for a given eccentricity and observing angle, while accretion-rate variability for eccentric orbits encodes the binary phase via accretion-rate peaks that occur near pericenter for prograde orbits and between pericenter and apocenter for retrograde orbits (see Figure 2).

In contrast, for a near-circular-orbit binary, the peak of orbital timescale variability is related to the passage of a binary component by the nearside of the lopsided circumbinary cavity (e.g., D. J. D'Orazio et al. 2013) and so depends on the relative orientation of the cavity and not the binary phase with respect to the observer's line of sight. Put another way, a lightcurve exhibiting hydrodynamic and Doppler +lensing variability for a near-circular-orbit binary would only allow identification up to an undetermined orientation of the CBD cavity on the sky. For an eccentric binary this free parameter is eliminated, and the lightcurve model is fully specified by binary parameters and the observer's viewing angle.

That the lightcurves in Figures 6 and 7 are unique to the chosen binary parameters and observer angles offers considerable constraining power compared to the circular-orbit case. It also makes this signature more difficult to duplicate via non-SMBHB drivers of variability. The detectability of such features depends on the sensitivity and cadence of observations but is promising for a Vera Rubin Observatory, LSST-like survey and the Doppler-plus-lensing signatures from SMBHBs studied in L. Z. Kelley et al. (2021) and K. Park et al. (2024).

Finally, we note that for equal-mass binaries it is often assumed that the orbital Doppler effect is nullified or greatly diminished since both black hole minidisks are assumed to be emitting at the same luminosity and, via the two-body problem, will have opposite line-of-sight velocities (e.g., D. J. D'Orazio et al. 2015). However, because the accretion rate can be split unequally between the components of eccentric binaries (Figure 5), the Doppler boost can still cause significant modulations for equal-mass binaries when the orbital eccentricity is nonzero.

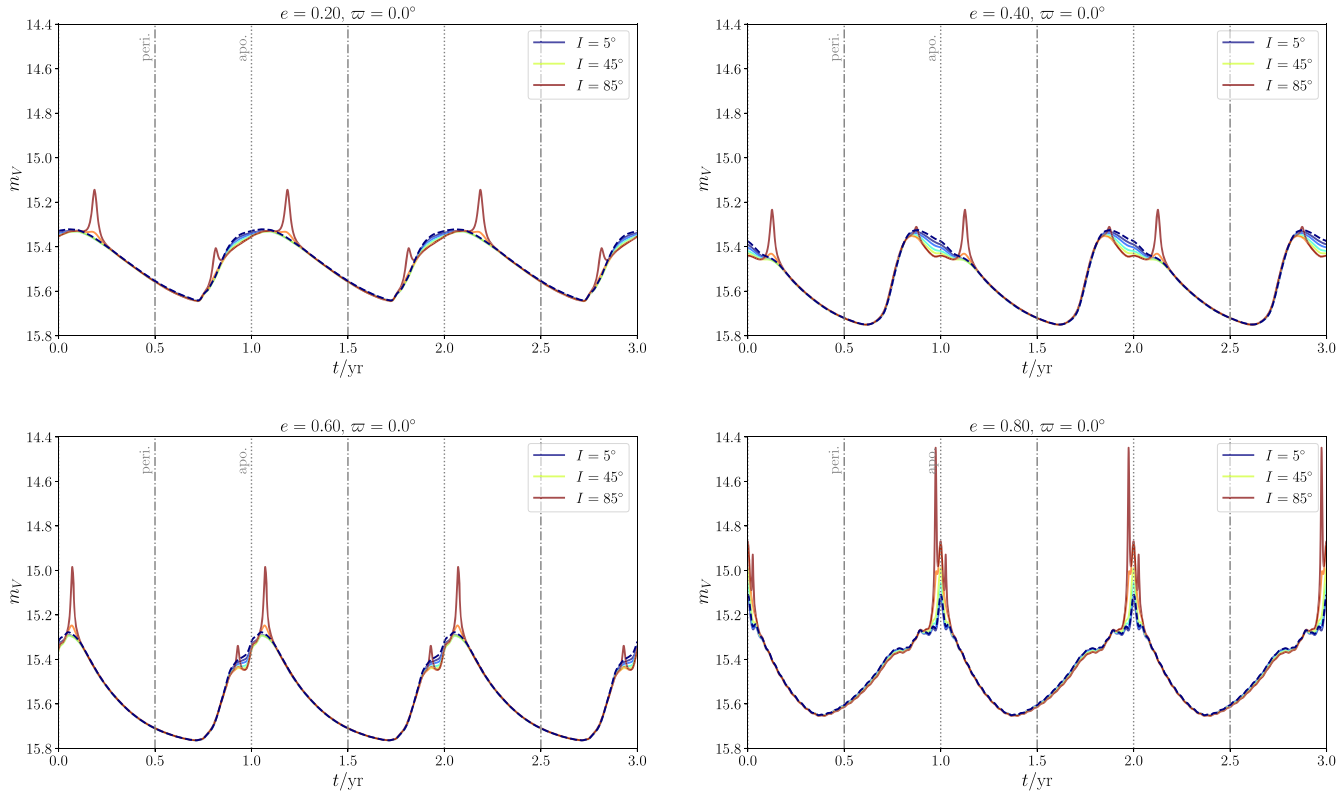


**Figure 7.** The same as Figure 6, except each panel is for a different binary orbital eccentricity and the same viewing azimuth. Note that, as in Figure 6, viewing angles $\varpi$ and $I$ affect only the Doppler boost and lensing signatures, while the binary eccentricity affects both accretion variability and Doppler+lensing magnifications.

## 5. Discussion and Conclusion

We have analyzed the variability (Figure 1) and relative magnitudes (Figure 5) of accretion rates measured from viscous hydrodynamical simulations of disks accreting onto equal-mass, eccentric binaries in both prograde and retrograde configurations. With the goal of generating lightcurve models to facilitate searches for accreting binaries, we developed a tool, named `binlite`, which can rapidly generate accretion-rate time series at any eccentricity in our continuous sweep of simulations ($e \leqslant 0.8$). We then postprocessed these accretion-rate time series to generate simple models for lightcurves at optical wavelengths, including also observer-dependent effects of orbital Doppler boosting and gravitational self-lensing.

It is important to note that the details of the accretion rates presented here will likely vary with different included physics, sink prescriptions, and numerical methods for solving the equations of hydrodynamics. However, while these simulations correspond to a simplest nontrivial inclusion of 2D, viscous, isothermal hydrodynamics, they capture some robust features that lead to accretion-rate periodicities observed over a wide range of calculations that include different physics: 3D (e.g., M. S. L. Moody et al. 2019), self-gravity (A. Franchini et al. 2024b), magnetohydrodynamics (MHD; e.g., J.-M. Shi et al. 2012; J.-M. Shi & J. H. Krolik 2015), general relativity (e.g., S. C. Noble et al. 2021), nonisothermal equations of state (e.g., R. Günther & W. Kley 2002; J. R. Westernacher-Schneider et al. 2022; H.-Y. Wang et al. 2023), for fixed and live binaries (e.g., A. Franchini et al. 2023), and are robust over a wide range of numerical techniques (P. C. Duffell et al. 2024). Hence, while exact shapes of accretion-rate times series will depend on the physical parameters and numerical methods employed, the accretion-rate times series available through `binlite` can give insight into the types of accretion variability expected and aid in building templates with which to search for such signatures.

Furthermore, the simple lightcurve models presented in Section 4 could be expanded and adapted to numerous situations. More complex spectra that take into account different accretion flow properties could be added to this picture, e.g., emission characteristics of radiatively inefficient accretion flows (see the Methods Section of D. J. D'Orazio et al. 2015), or those tailored to protoplanetary disks (e.g., Z. Zhu 2015). Timescales for the disk spectra to respond to the changing accretion rate could also be taken into account. For example, the lightcurve generation procedure presented here could be modified by smoothing the reconstructed accretion rates in time with a smoothing kernel set by a buffering timescale due to, e.g., photon diffusion. Beyond this, the fluid properties of the disk (via postprocessing or inclusion of radiative cooling terms in the energy equation) can be used to generate mock spectra, as has been done for a much smaller parameter space in a number of works using viscous hydrodynamics (e.g., B. D. Farris et al. 2015; Y. Tang et al. 2018; J. R. Westernacher-Schneider et al. 2022; L. M. Krauth et al. 2023; F. Cocchiararo et al. 2024; A. Franchini et al. 2024a), as well as general relativistic MHD (e.g.,S. d'Ascoli et al. 2018; L. Combi et al. 2022; E. M. Gutiérrez et al. 2022; M. J. Avara et al. 2024).

In addition to advancing lightcurve models with the accretion-rate time series investigated here, the accretion rates accessible with this tool should also be updated with the newest, and a wider range of, simulation results. Utilizing both simple and fast simulations, which will expand available data to a wider range of parameter space (e.g., a wider range of binary and disk parameters for the types of simulations analyzed here;

D. J. D'Orazio et al. 2016; C. Tiede et al. 2020; A. J. Dittmann & G. Ryan 2022, 2024), and also simulations including more physics that can improve accuracy in smaller portions of parameter space, we plan to add such improvements over time from our own calculations and also from the wider community.

## 6. Public Availability : `binlite`

We have developed a simple Python package for rapidly generating periodic accretion-rate time series and associated flux series at any eccentricity in our continuous sweep simulations.

`binlite` is available in the Python Package Index, and it can be installed with

```
python -m pip install binlite
```

and imported locally as

```
import binlite as blt.
```

It contains two main modules:

```
blt.accretion
blt.flux
```

for generating variability series of the mass accretion onto the binary and the flux at a given frequency (under the assumptions detailed in Section 4), respectively. The source code and more detailed documentation are also available at github.com/nbia-gwastro/binlite and as a frozen release at doi:10.5281/zenodo.13984289.

## Acknowledgments

D.J.D. received funding from the European Union's Horizon 2020 research and innovation program under Marie Sklodowska-Curie grant agreement No. 101029157. D.J.D. and C.T. acknowledge support from the Danish Independent Research Fund through Sapere Aude Starting grant No. 121587. P.D. acknowledges support from the National Science Foundation under grant AAG-2206299. C.T. also received support from the European Unions Horizon 2023 research and innovation program under Marie Sklodowska-Curie grant agreement No. 10114836. This work was supported in part by grant NSF PHY-1748958 to the Kavli Institute for Theoretical Physics (KITP) and carried out in part through the KITP program "Bridging the Gap: Accretion and Orbital Evolution in Stellar and Black Hole Binaries" (https://www.kitp.ucsb.edu/activities/binary22). The authors thank the anonymous referee.

## ORCID iDs

Daniel J. D'Orazio https://orcid.org/0000-0002-1271-6247
Paul C. Duffell https://orcid.org/0000-0001-7626-9629
Christopher Tiede https://orcid.org/0000-0002-3820-2404

## References

Alves, F. O., Caselli, P., Girart, J. M., et al. 2019, Sci, 366, 90
Avara, M. J., Krolik, J. H., Campanelli, M., et al. 2024, ApJ, 974, 242
Begelman, M. C., Blandford, R. D., & Rees, M. J. 1980, Natur, 287, 307
Charisi, M., Haiman, Z., Schiminovich, D., & D'Orazio, D. J. 2018, MNRAS, 476, 4617
Charisi, M., Taylor, S. R., Runnoe, J., Bogdanovic, T., & Trump, J. R. 2022, MNRAS, 510, 5929
Cocchiararo, F., Franchini, A., Lupi, A., & Sesana, A. 2024, A&A, 691, A250
Combi, L., Lopez Armengol, F. G., Campanelli, M., et al. 2022, ApJ, 928, 187
Czekala, I., Ribas, Á., Cuello, N., et al. 2021, ApJ, 912, 6
d'Ascoli, S., Noble, S. C., Bowen, D. B., et al. 2018, ApJ, 865, 140
Davelaar, J., & Haiman, Z. 2022, PhRvD, 105, 103010
Dempsey, A. M., Muñoz, D., & Lithwick, Y. 2020, ApJL, 892, L29
Dittmann, A. J., & Ryan, G. 2021, ApJ, 921, 71
Dittmann, A. J., & Ryan, G. 2022, MNRAS, 513, 6158
Dittmann, A. J., & Ryan, G. 2024, ApJ, 967, 12
D'Orazio, D., Duffell, P., & Tiede, C. 2024, binlite v1.1.1, Zenodo, doi:10.5281/zenodo.13984289
D'Orazio, D. J., & Charisi, M. 2023, arXiv:2310.16896
D'Orazio, D. J., & Di Stefano, R. 2018, MNRAS, 474, 2975
D'Orazio, D. J., & Duffell, P. C. 2021, ApJL, 914, L21
D'Orazio, D. J., Haiman, Z., Duffell, P., MacFadyen, A., & Farris, B. 2016, MNRAS, 459, 2379
D'Orazio, D. J., Haiman, Z., & MacFadyen, A. 2013, MNRAS, 436, 2997
D'Orazio, D. J., Haiman, Z., & Schiminovich, D. 2015, Natur, 525, 351
D'Orazio, D. J., & Loeb, A. 2018, ApJ, 863, 185
D'Orazio, D. J., & Loeb, A. 2019, PhRvD, 100, 103016
Duffell, P. C. 2016, ApJS, 226, 2
Duffell, P. C., D'Orazio, D., Derdzinski, A., et al. 2020, ApJ, 901, 25
Duffell, P. C., Dittmann, A. J., D'Orazio, D. J., et al. 2024, ApJ, 970, 156
Dunhill, A. C., Cuadra, J., & Dougados, C. 2015, MNRAS, 448, 3545
Farris, B. D., Duffell, P., MacFadyen, A. I., & Haiman, Z. 2014, ApJ, 783, 134
Farris, B. D., Duffell, P., MacFadyen, A. I., & Haiman, Z. 2015, MNRAS, 446, L36
Farris, B. D., Gold, R., Paschalidis, V., Etienne, Z. B., & Shapiro, S. L. 2012, PhRvL, 109, 221102
Franchini, A., Bonetti, M., Lupi, A., & Sesana, A. 2024a, A&A, 686, A288
Franchini, A., Lupi, A., Sesana, A., & Haiman, Z. 2023, MNRAS, 522, 1569
Franchini, A., Prato, A., Longarini, C., & Sesana, A. 2024b, A&A, 688, A174
Günther, R., & Kley, W. 2002, A&A, 387, 550
Gutiérrez, E. M., Combi, L., Noble, S. C., et al. 2022, ApJ, 928, 137
Haiman, Z., Kocsis, B., & Menou, K. 2009, ApJ, 700, 1952
Haiman, Z., Xin, C., Bogdanović, T., et al. 2023, arXiv:2306.14990
Hayasaki, K., Mineshige, S., & Ho, L. C. 2008, ApJ, 682, 1134
Hu, B. X., D'Orazio, D. J., Haiman, Z., et al. 2020, MNRAS, 495, 4061
Ingram, A., Motta, S. E., Aigrain, S., & Karastergiou, A. 2021, MNRAS, 503, 1703
Kelley, L. Z., D'Orazio, D. J., & Di Stefano, R. 2021, MNRAS, 508, 2524
Krauth, L. M., Davelaar, J., Haiman, Z., et al. 2023, MNRAS, 526, 5441
Krauth, L. M., Davelaar, J., Haiman, Z., et al. 2024, PRD, 109, 103014
Lai, D., & Muñoz, D. J. 2023, ARA&A, 61, 517
MacFadyen, A. I., & Milosavljević, M. 2008, ApJ, 672, 83
Miranda, R., Munoz, D. J., & Lai, D. 2017, MNRAS, 466, 1170
Moody, M. S. L., Shi, J.-M., & Stone, J. M. 2019, ApJ, 875, 66
Muñoz, D. J., & Lai, D. 2016, ApJ, 827, 43
Muñoz, D. J., Miranda, R., & Lai, D. 2019, ApJ, 871, 84
Nelson, R. P. 2018, in Handbook of Exoplanets, ed. H. J. Deeg & J. A. Belmonte (Berlin: Springer), 139
Noble, S. C., Krolik, J. H., Campanelli, M., et al. 2021, ApJ, 922, 175
Park, K., Xin, C., Davelaar, J., & Haiman, Z. 2024, arXiv:2409.04583
Roedig, C., Krolik, J. H., & Miller, M. C. 2014, ApJ, 785, 115
Shi, J.-M., & Krolik, J. H. 2015, ApJ, 807, 131
Shi, J.-M., Krolik, J. H., Lubow, S. H., & Hawley, J. F. 2012, ApJ, 749, 118
Siwek, M., Weinberger, R., & Hernquist, L. 2023a, MNRAS, 522, 2707
Siwek, M., Weinberger, R., Muñoz, D. J., & Hernquist, L. 2023b, MNRAS, 518, 5059
Stone, N. C., Metzger, B. D., & Haiman, Z. 2017, MNRAS, 464, 946
Tang, Y., Haiman, Z., & MacFadyen, A. 2018, MNRAS, 476, 2249
Tiede, C., & D'Orazio, D. J. 2024, MNRAS, 527, 6021
Tiede, C., Zrake, J., MacFadyen, A., & Haiman, Z. 2020, ApJ, 900, 43
Tobin, J. J., Kratter, K. M., Persson, M. V., et al. 2016, Natur, 538, 483
Tofflemire, B. M., Mathieu, R. D., Ardila, D. R., et al. 2017a, ApJ, 835, 8
Tofflemire, B. M., Mathieu, R. D., Herczeg, G. J., Akeson, R. L., & Ciardi, D. R. 2017b, ApJL, 842, L12
Valli, R., Tiede, C., Vigna-Gómez, A., et al. 2024, A&A, 688, A128
Vaughan, S., Uttley, P., Markowitz, A. G., et al. 2016, MNRAS, 461, 3145
Wang, H.-Y., Bai, X.-N., Lai, D., & Lin, D. N. C. 2023, MNRAS, 526, 3570
Ward, W. R. 1997, Icar, 126, 261
Westernacher-Schneider, J. R., Zrake, J., MacFadyen, A., & Haiman, Z. 2022, PhRvD, 106, 103010
Witt, C. A., Charisi, M., Taylor, S. R., & Burke-Spolaor, S. 2022, ApJ, 936, 89
Xin, C., & Haiman, Z. 2021, MNRAS, 506, 2408
Xin, C., & Haiman, Z. 2024, MNRAS, 533, 3164
Zhu, X.-J., & Thrane, E. 2020, ApJ, 900, 117
Zhu, Z. 2015, ApJ, 799, 16
Zrake, J., Tiede, C., MacFadyen, A., & Haiman, Z. 2021, ApJL, 909, L13
Zurlo, A., Gratton, R., Perez, S., & Cieza, L. 2023, EPJP, 138, 411